# Electrochemical Sensor Based on a Composite of Reduced Graphene Oxide and Molecularly Imprinted Copolymer of Polyaniline−Poly(o-phenylenediamine) for Ciprofloxacin Determination: Fabrication, Characterization, and Performance Evaluation

Jedsada Chuiprasert, Sira Srinives, Narin Boontanon, Chongrak Polprasert, Nudjarin Ramungul, Napat Lertthanaphol, Apisit Karawek, and Suwanna Kitpati Boontanon*

Read Online

ACCESS | Metrics & More | Article Recommendations | Supporting Information

**ABSTRACT:** Contamination of antibiotics in water is a major cause of antibiotic resistance (ABR) in pathogens that endangers human health and food security worldwide. Ciprofloxacin (CIP) is a synthetic fluoroquinolone (FQ) antibiotic and is reportedly present in surface water at a concentration exceeding the ecotoxicological predicted no-effect concentration in some areas. This study fabricated a CIP sensor using an electropolymerized molecularly imprinted polymer (MIP) of polyaniline (PANI) and poly(o-phenylenediamine) (o-PDA) with CIP recognition sites. The MIP was coated on a reduced graphene oxide (rGO)-modified glassy carbon electrode (rGO/GCE) and operated under a differential pulse voltammetry (DPV) mode for CIP detection. The sensor exhibited an excellent response from $1.0 \times 10^{-9}$ to $5.0 \times 10^{-7}$ mol L$^{-1}$ CIP, showing a sensor detection limit and sensitivity of $5.28 \times 10^{-11}$ mol L$^{-1}$ and 5.78 $\mu$A mol$^{-1}$ L, respectively. The sensor's sensitivity for CIP was 1.5 times higher than that of the other tested antibiotics, including enrofloxacin (ENR), ofloxacin (OFX), sulfamethoxazole (SMZ), and piperacillin sodium salt (PIP). The reproducibility and reusability of the sensor devices were also studied.
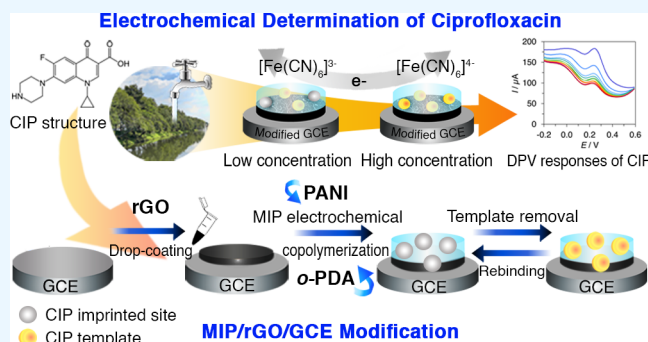
## 1. INTRODUCTION

Ciprofloxacin (CIP) is a synthetic second-generation fluoroquinolone (FQ) antibiotic used to prevent and treat infectious bacterial diseases. It is a widely used medicine for humans and veterinary use, providing excellent bactericidal responses against gram-negative and gram-positive pathogens. Generally, more than 75% of the consumed CIP is unmetabolized and excreted into the environment, polluting surface water, groundwater, and drinking water.[1,2] Several reports reveal the presence of ng L$^{-1}$ to $\mu$g L$^{-1}$ CIP in wastewater at water treatment facilities, which contributes to antibiotic resistance (ABR) in pathogens and leads to difficult-to-treat or even untreatable infections. The issue of ABR has become a global concern that requires urgent action to reduce the impact and control the expansion of resistance.[3]

Several analytical methods were employed to determine CIP in water, including high-performance liquid chromatography (HPLC),[4] fluorescence spectrophotometry,[5] atomic absorption spectrometry, and capillary electrophoresis.[6] Although these techniques are standardized and reliable, they require costly instruments, are time-consuming, and are impractical for on-site monitoring. Therefore, a mobile sensing device that provides quick concentration measurements at a reasonable price is essential. An electrochemical sensor is a monitoring device that relies on redox reactions to yield sensing responses to a target analyte. Such a device can be used as an alternative to conventional techniques for detecting CIP with a quick response time, the potential to be installed in a compact area, and excellent mobility for on-site measurements.

The molecularly imprinted polymer (MIP) is a technique that carries specific sites for a target molecule using the molecule as the template. It has recently received significant attention owing to its high selectivity and sensitivity toward

targets. Applications of MIP have been demonstrated in drug delivery,[7,8] solid-phase extraction coupled with liquid chromatography,[9,10] catalysis,[11,12] and environmental and biomedical sensing.[13−15] Various techniques have been utilized to synthesize MIP layers, including free-radical polymerization, chemical grafting,[16] soft lithographies,[17] molecular self-assembly,[18] and electropolymerization.[19,20] Among these techniques, electropolymerization is a practical approach for MIP synthesis because a target molecule can be added to the electrolyte and entrapped in a conductive polymeric film. The molecules are sequentially extracted or leached out of the external polymeric surfaces to create recognition sites for MIP. Yahyapour et al.[21] synthesized MIP from the 4-aminobenzoic acid in the presence of a cometal organic framework nanofiber. The composite was coated on a glassy carbon electrode (GCE) and operated in differential pulse voltammetry (DPV) to exhibit sensitivity and a limit of detection (LOD) of 0.016 $\mu$A $\mu$mol$^{-1}$ L and $1.7 \times 10^{-8}$ mol L$^{-1}$ for CIP detection. Jiang et al.[22] electropolymerized $o$-phenylenediamine ($o$-PDA) and L-lysine using cyclic voltammetry (CV) mode with a moxifloxacin template. The poly L-lysine-$o$-PDA copolymer MIP showed sensitivity and LOD of 11.3 $\mu$A mol$^{-1}$ L and $5.12 \times 10^{-10}$ mol L$^{-1}$, respectively, for moxifloxacin. The synergic effects of L-lysine-$o$-PDA were the key to the excellent performance of the MIP as a sensitive element. El Azab et al.[23] synthesized a poly(levodopa) and poly($o$-phenylenediamine) composite onto gold nanoparticles. The composite was utilized as a sensor in the detection of levofloxacin. The sensor operated in the DPV mode provided a sensitivity of 356,955 $\mu$A mol$^{-1}$ L and had an LOD of $4.62 \times 10^{-7}$ mol L$^{-1}$.

Polyaniline (PANI) is a popular conductive polymer, offering a wide range of tunable conductivities, and is electroactive in acidic to neutral pH ranges.[24,25] It can be copolymerized with other conductive polymers, such as $o$-PDA, to combine functionality and adjust the conductivity of the copolymer film. The copolymer of PANI and $o$-PDA integrates the excellent conductivity of PANI and the thin-film-forming nature of $o$-PDA, making it a great candidate for MIP. An issue regarding the film is the passivation of the entrapped nonconductive molecules during electropolymerization. This causes an over-oxidation of the conductive polymer film, which leads to poor surface electroactivity at the external layer.

Carbon nanostructures with high charge-transfer ability, such as carbon nanotubes and reduced graphene oxide (rGO), can be implemented in the MIP to enhance the electroactivity of the MIP film. Graphene is a two-dimensional nanostructure with chemical stability, good charge-transfer ability, and outstanding electroactivity. It can be synthesized on a gram scale following a chemical exfoliation method that yields GO, a graphene sheet with few carbon layers and many functional groups. The functional groups on GO are structural defects that inhibit the charge mobility through the GO sheet and cause GO to be electrically insulating. GO can be chemically reduced to remove some functional groups and form rGO, a semiconductive material. rGO is a popular transducer and has been demonstrated as a sensitive element for charge-transfer enhancement in electrochemical sensors.[26−31]

In this study, we synthesized PANI−$o$-PDA MIP/rGO on a GCE and used it as the working electrode (WE) in an electrochemical sensor. The rGO was coated on GCE followed by the electro-copolymerization of PANI−$o$-PDA MIP film. CIP was added to the electrolyte during the electro-copolymerization and later removed to create recognition

sites on the MIP. The sensor was characterized using CV and exploited in the DPV mode for CIP measurement. We compared CIP measurement results from the MIP/rGO/GCE with those of the non MIP (NIP)/rGO/GCE. In addition, the MIP/rGO/GCE sensor was tested against other antibiotics, including enrofloxacin (ENR), ofloxacin (OFX), sulfamethoxazole (SMZ), and piperacillin sodium salt (PIP), for cross-sensitivity studies.

## 2. RESULTS AND DISCUSSION

### 2.1. Physical and Chemical Characterizations.

*2.1.1. Physical Characterizations.* CIP, rGO, pre-elution MIP/rGO, and post-elution MIP/rGO were observed by field-emission scanning electron microscopy (FE-SEM). CIP (Figure 1A) appears to be a rod-shaped crystal structure with
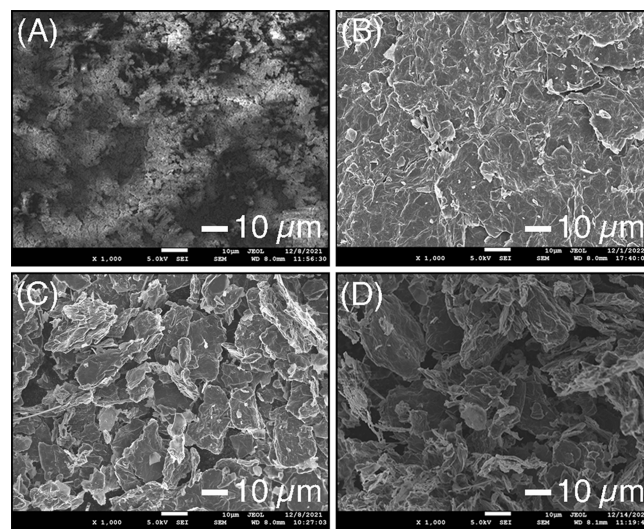


**Figure 1.** FE-SEM images of (A) CIP, (B) rGO, (C) pre-elution MIP/rGO, and (D) post-elution MIP/rGO.

an average diameter and length of $368.0 \pm 101.6$ and $1088.0 \pm 130.8$ nm, respectively. rGO (Figure 1B) is a sheet-like structure that promotes the formation of self-assembled films. The pre-elution MIP/rGO (Figure 1C) shows the MIP copolymer film coated on rGO sheets, in which the CIP structure is hardly distinguishable from other substances. Surface roughness and thickness increase slightly compared to rGO owing to the film coverage of the CIP−PANI−$o$-PDA copolymer. The post-elution MIP/rGO exhibits wrinkles, roughness (Figure 1D), and a sheet-like structure resulting from CIP elution.

*2.1.2. FT-IR Spectral Studies.* FT-IR spectra revealed the presence of functional groups in the synthesized GO, rGO, NIP, post-elution NIP/rGO, and post-elution MIP/rGO (Figure 2A) samples. The spectra of GO and rGO exhibited a broad peak at 3408 cm$^{-1}$, corresponding to the stretching vibrations of hydroxyl (O−H) and moisture. Weak bands at 2919 and 2851 cm$^{-1}$ were attributed to the residual alkyl groups (C−H).[33] FT-IR spectrum of rGO is slightly less intense than that of the GO because of the partial removal of the functional groups from the GO. NIP was the PANI−$o$-PDA copolymer with no CIP and was tested as a control sample. The FT-IR peaks for the NIP in the 3200−3500 cm$^{-1}$ were attributed to the N−H stretching vibrations of secondary amine on the PANI−$o$-PDA.[34] The peaks at 2600, 1625, and
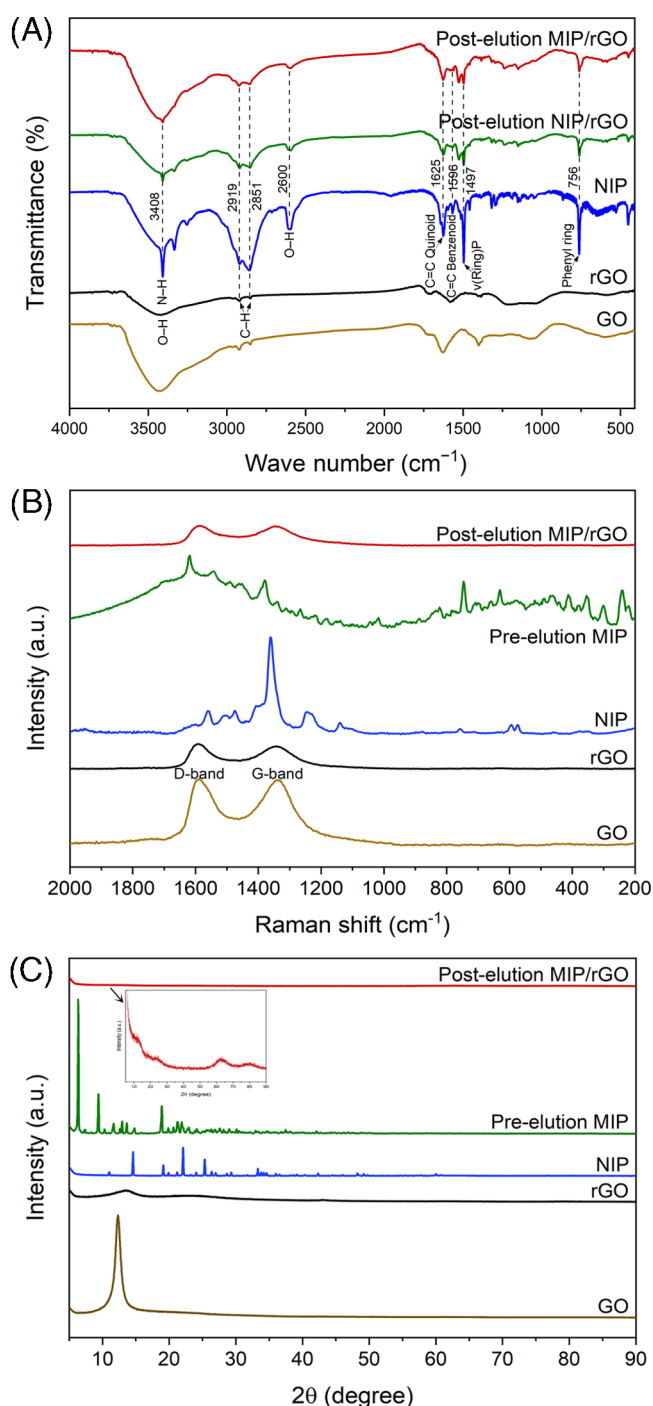
**Figure 2.** (A) FT-IR spectra of GO, rGO, NIP, post-elution NIP/rGO, and post-elution MIP/rGO; (B) Raman spectra of GO, rGO, NIP, pre-elution MIP, and post-elution MIP/rGO; and (C) XRD spectra of GO, rGO, NIP, pre-elution MIP, and post-elution MIP/rGO.

groups on the copolymer and rGO. The copolymer (NIP and MIP) of the NIP/rGO and MIP/rGO provided peak signals at 1625, 1598, 1497, and 756 cm$^{-1}$, corresponding to the C=C vibrations of quinoid, C=C vibrations of benzenoid, phenazine, and phenyl ring, respectively.

*2.1.3. Raman and X-ray Diffraction (XRD) Analysis.* Raman spectroscopy is an effective tool for characterizing rGO because it provides information on the disordered amorphous structure and ordered graphitic structure ratio ($I_D/I_G$). For GO, rGO, and post-elution MIP/rGO, the $I_G$ and $I_D$ bands were present at 1340 and 1589 cm$^{-1}$. The $I_D/I_G$ for GO, rGO, and post-elution MIP/rGO was 0.98, 0.91, and 0.94, respectively (Figure 2B), revealing an equivalent level of crystallinity. For NIP, the spectral peak at 1360 and 1514 cm$^{-1}$ corresponded to the C−N•+ stretching of delocalized polaronic charge carriers and the N−H bending deformation of protonated amines.[36] For the pre-elution MIP, the peaks at 1618 and 1379 cm$^{-1}$ corresponded to the C−C stretching of an aromatic ring and a combination of CH$_2$ wagging and C−C stretching. The Raman spectra confirm that the composite contains copolymer and graphene; both phases maintain their functionalities and crystallinities.

The crystallographic structures of GO, rGO, NIP, pre-elution MIP, and post-elution MIP/rGO were studied using XRD (Figure 2C). For GO, the pattern showed only one broad peak at $2\theta = 12.3°$, corresponding to the (001) plane of the graphene structure.[37] For rGO, two broad peaks were observed at 14° and 24°, corresponding to the (001) and (002) planes of rGO. For NIP, the XRD patterns at 14.6°, 22.1°, 25.3°, and 33.3° were observed, suggesting the presence of PANI and poly($o$-PDA).[38−40] For pre-elution MIP, the XRD patterns were observed at 6.3°, 9.4°, and 18.9°, indicating the presence of the copolymer PANI and poly($o$-PDA). Notably, the copolymer pattern was shifted from its initial position, and other small peaks were observed. The shift can be attributed to the presence of CIP in the copolymer matrix.[41] For the post-elution MIP/rGO, signals from the rGO pattern overlapped with the copolymer, resulting in only one broad peak at 15.1°.

**2.2. Electrochemical Characterization.** Electrochemical currents from CV analysis were used to investigate the electroactivity of the modified electrodes in a background mediator of $[Fe(CN)_6]^{3−/4−}$. The anodic and cathodic peaks of the bare GCE were observed at 0.26 and 0.11 V (Figure 3A). The height of the anodic peak was extracted as the response
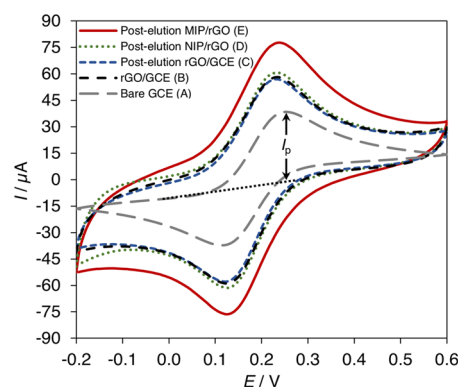


**Figure 3.** Electroactivity of the bare GCE (A), rGO/GCE (B), post-elution rGO/GCE (C), post-elution NIP/rGO/GCE (D), post-elution MIP/rGO/GCE (E), and in $[Fe(CN)_6]^{3−/4−}$ mediator evaluated by CV at scan rate of 50 mV s$^{-1}$ ($n = 5$).

1598 cm$^{-1}$ corresponded to O−H of the carboxyl group, C=C vibrations of quinoid, and C=C vibrations of benzenoid, respectively. The absorption band at 1497 cm$^{-1}$ could be ascribed to the phenazine group,[35] whereas the peak at 756 cm$^{-1}$ was associated with the substituted phenyl ring. The post-elution NIP/rGO and post-elution MIP/rGO samples provided a similar IR pattern. The peaks at 3424, 2919, 2851, and 2600 cm$^{-1}$ corresponded to N−H, C−H, C−H, and O−H groups, respectively, and were contributed by the functional

**Figure 4.** EDS pattern of the pre-elution MIP/rGO (A) and post-elution MIP/rGO (B); changes in $I_p$ corresponding to different template removal eluents used in the preparation of MIP/rGO/GCE (C).

($I_p$). The $I_p$ values for the bare GCE and rGO/GCE were 38.27 and 58.08 $\mu$A, respectively, indicating a significant enhancement in charge-transfer ability owing to the incorporation of rGO (Figure 3B). The post-elution rGO/GCE (Figure 3C) exhibited an $I_p$ value of 56.92 $\mu$A, indicating no effect from the elution process on the electroactivity of rGO/GCE. For NIP/rGO/GCE (Figure 3D), $I_p$ was 60.79 $\mu$A, slightly higher than that of rGO/GCE and post-elution rGO/GCE. We believe that NIP, a copolymer film of PANI−$o$-PDA, can provide an extra surface area for the electrode or a reduction in the double layer of the electrode/copolymer interfaces. The post-elution MIP/rGO/GCE (Figure 3E) produced the highest $I_p$ of 77.77 $\mu$A, which is attributed to an additional surface area from wrinkles and a sheet-like copolymer of the MIP. We determined the electroactive area of the electrode following the Randles−Sevcik equation (eq 1):[32,42]

$$I_p = (2.69 \times 10^5)AD^{1/2}n^{3/2}v^{1/2}C \tag{1}$$

where $I_p$ denotes the anodic peak current (A), $A$ denotes the electroactive area (cm$^2$), $D$ denotes the diffusion coefficient ($4.0 \times 10^{-6}$ cm$^2$ s$^{-1}$), $n$ denotes the number of electrons participating in the redox reaction ($n$ = 1), $v$ denotes the scan rate (V s$^{-1}$), and $C$ denotes the concentrati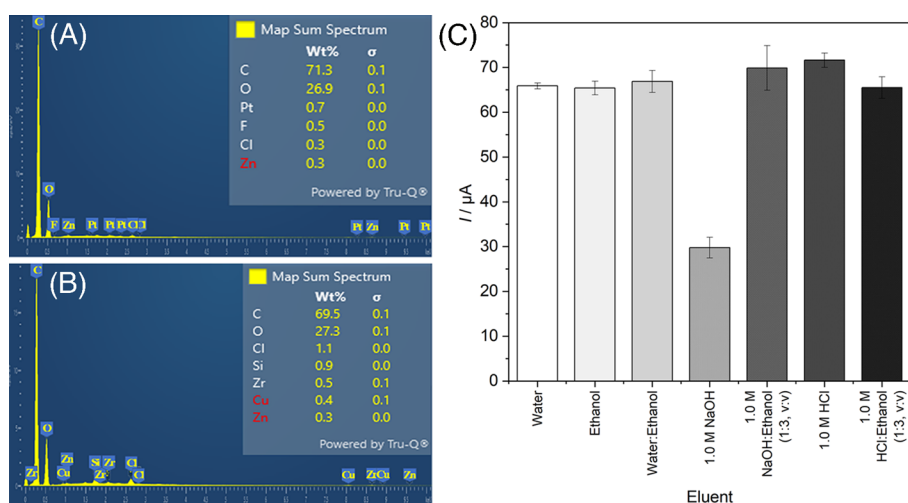on of the probe molecule ($5.0 \times 10^{-3}$ mol L$^{-1}$ [Fe(CN)$_6$]$^{3-/4-}$). The electroactive areas of bare GCE, rGO/GCE, post-elution rGO/GCE, post-elution NIP/rGO/GCE, and post-elution MIP/rGO/GCE were 0.07, 0.09, 0.09, 0.10, and 0.14 cm$^2$, respectively.

**2.3. Variation in MIP/rGO/GCE Synthesis Conditions.**
*2.3.1. Effect of the Suspension Medium of rGO.* The rGO can be suspended in water and a polar aprotic solvent such as dimethylformamide (DMF). The effect of the suspension medium was studied by suspending rGO in either ultrapure water (UPW) or DMF at a concentration of 1.0 mg mL$^{-1}$. The suspension was drop-coated onto GCE. The electroactivity of rGO/GCE was investigated in the CV mode (Figure S1a). The rGO (UPW)/GCE and rGO (DMF)/GCE provided $I_p$ values of 54.56 and 48.42 $\mu$A, respectively. The GO (UPW)/GCE was studied as a control sample and yielded an $I_p$ of 1.25 $\mu$A. Based on the $I_p$ results, rGO suspension in UPW medium was used for subsequent experiments.

*2.3.2. Effect of pH in Electropolymerization.* The pH of electrolytes plays a critical role in the electropolymerization of PANI and poly($o$-PDA). Because the ANI and $o$-PDA are electroactive in the pH range of 1−4, the experiments were performed accordingly. The MIP was electropolymerized on rGO/GCE from the electrolytes in the pH range of 1−4 to obtain the MIP/rGO/GCE. The MIP/rGO/GCE was characterized using a CV to receive the $I_p$ responses. The $I_p$ of MIP/rGO/GCE (Figure S1b) slightly increased from 55.46 to 59.43 and 60.71 $\mu$A as the pH increased from 1 to 3. Furthermore, the $I_p$ decreased to 55.87 $\mu$A when the pH of the electrolyte reached beyond 3.5. The results support the hypothesis that the copolymer is only well electropolymerized within the potential pH range. The dependence of MIP electropolymerization on the pH of electrolytes results from a surface cavity, oxidative state, and surface structure of the copolymer film. Therefore, a medium solution (pH 3.0) was selected for the electropolymerization of the MIP.

*2.3.3. Effect of CIP Concentration.* CIP was used as a template for MIP synthesis. The concentration of CIP in the electrolytes can significantly affect the number of cavities on MIP. To investigate the effect of template concentration, MIP was polymerized on rGO/GCE at different CIP concentrations, ranging from $1.0 \times 10^{-3}$ to $10.0 \times 10^{-3}$ mol L$^{-1}$ (Figure S1c) (pH of electrolytes = 3). At CIP concentrations of $1.0 \times 10^{-3}$ and $2.5 \times 10^{-3}$ mol L$^{-1}$, the $I_p$ values were 60.02 and 60.29 $\mu$A, respectively. The highest $I_p$ of 63.71 $\mu$A was obtained for MIP/rGO synthesized at a CIP concentration of $5.0 \times 10^{-3}$ mol L$^{-1}$. As the CIP concentration increased to $7.5 \times 10^{-3}$ and $10 \times 10^{-3}$ mol L$^{-1}$, the $I_p$ value decreased to 59.61 and 57.66 $\mu$A, respectively. This observation can be explained since CIP is less electroactive than the rGO and MIP, and excessive CIP coverage on MIP passivates the electroactive area and reduces the $I_p$ value.

*2.3.4. Effect of the Monomer Concentration.* The interaction between the monomers and CIP is essential to form a MIP film. During the electropolymerization, the ANI to $o$-PDA ratio varied from 2:1 to 1:1, 1:2, 1:3, 1:4, and 1:5. As the ANI to $o$-PDA ratio decreased from 2:1 to 1:1, $I_p$ increased from 56.88 to 59.88 $\mu$A (Figure S1d). This result explains the higher electroactivity of PANI than that of poly($o$-PDA), which leads to a thicker copolymer film and lower $I_p$ value. A
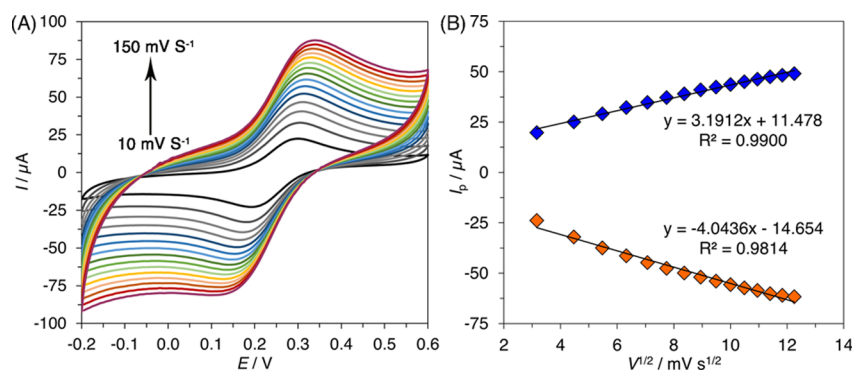
**Figure 5.** (A) CV of MIP/rGO/GCE at scan rates of 10 to 150 mV s$^{-1}$ and (B) plot of $I_p$ vs $\nu^{1/2}$ ($n = 5$).

decrease in $I_p$ value (52.26 $\mu$A) occurred as the ratio increased to 1:2. The $I_p$ value decreased to 52.62, 48.16, and 48.94 $\mu$A as the ratio decreased from 1:2 to 1:3, 1:4, and 1:5, respectively. This lowering of $I_p$ was attributed to the incorporation of poly(o-PDA) in the MIP/rGO, which reduced the electroactivity of the copolymer film. The ANI:o-PDA ratio of 1:1 was selected for the electropolymerization of the MIP.

*2.3.5. Effect of the Number of CV Cycles and Scan Rate.* In the electropolymerization of PANI−o-PDA copolymer, the number of cycles for the CV scan is crucial for the characteristics of the film. Electropolymerization was performed with cycle numbers ranging from 5 to 30 (Figure S1e). The film was employed as WE and studied for electroactivity in [Fe(CN)$_6$]$^{3-/4-}$ mediator. The number of cycles in electropolymerization process controls the thickness and electroactivity of the external layer of the MIP film.[33] As the number rose from 5 to 10 and 15, $I_p$ increased from 58.50 to 59.65 and 64.10 $\mu$A. This increasing trend ceased as $I_p$ decreased to 61.07, 57.15, and 50.57 $\mu$A, corresponding to the cyclic number of 20, 25, and 30, respectively. To investigate the effect of the scan rate on electropolymerization, MIP was electropolymerized in CV mode at different scan rates in the 30−100 mV s$^{-1}$ window. The $I_p$ was insensitive to the scan rate changes at 30, 40, 50, and 60 mV s$^{-1}$, a relatively low scan rate range (Figure S1f), yielding $I_p$ values of 64.23, 64.10, 64.50, and 64.20 $\mu$A, respectively. However, the $I_p$ rose more intensely at a high scan rate change of 70 to 80 mV s$^{-1}$, yielding $I_p$ values of 65.52 and 66.52 $\mu$A, respectively. A decrease in $I_p$ was observed as the scan rate increased to 100 mV s$^{-1}$ owing to insufficient monomer diffusion to the WE and over-oxidation of the external layer of the copolymer film. Thus, for the MIP synthesis, the number of CV cycles and the scan rate were set at 15 and 80 mV s$^{-1}$, respectively.

*2.3.6. Template Removal Eluents.* Removal of CIP from MIP was required to create CIP recognition sites on the MIP film. The removal process can be studied using EDS spectra comparing binding energy signals from the pre-eluted and post-eluted MIP/rGO/GCE. The signal from fluorine (F) revealed the presence of the CIP (Figure 4A). The CIP removal was performed by submerging MIP/rGO/GCE in a 1.0 mol L$^{-1}$ HCl solution for 180 s. The F signal was spotted at 0.70 eV for the pre-elution MIP/rGO and disappeared for the post-elution MIP/rGO (Figure 4B). The disappearance of the F signal indicates the absence of CIP on the MIP after the removal step. In this study, water, ethanol, water−ethanol mixture (1:3, v:v), 1.0 mol L$^{-1}$ NaOH, 1.0 mol L$^{-1}$ NaOH solution−ethanol mixture (1:3, v:v), 1.0 mol L$^{-1}$ HCl, and 1.0 mol L$^{-1}$ HCl solution−ethanol mixture (1:3, v:v) were tested

as eluting solutions (eluents) for template removal (Figure 4C). Water, ethanol, and the water−ethanol mixture provided MIP with $I_p$ values of 65.87, 65.41, and 66.87 $\mu$A, respectively. The 1.0 mol L$^{-1}$ NaOH yielded MIP with the lowest $I_p$ of 29.77 $\mu$A. However, MIP eluted with 1.0 mol L$^{-1}$ NaOH solution−ethanol mixture, 1.0 mol L$^{-1}$ HCl, and 1.0 mol L$^{-1}$ HCl solution−ethanol mixture provided $I_p$ values of 69.87, 71.60, and 65.49 $\mu$A, respectively. In this case, the solution interacts with copolymeric chains and causes the chains to release CIP. Differences in MIP electroactivities correspond to different eluents used in the CIP removal and correlate with the interactions between the copolymeric chains and the eluents.

*2.3.7. Time for CIP Removal.* Elution time is an essential factor for CIP removal and MIP synthesis. Figure S1g shows changes in the $I_p$ as the elution time varied from 30 to 300 s. The $I_p$ response plateaued quickly in the 70−72.55 $\mu$A range as the elution time rose from 30 to 150 s. The $I_p$ reached the maximum value of 76.42 $\mu$A at the elution time of 180 s and reduced to 67.44 and 66.59 $\mu$A as the elution time rose to 240 and 300 s.

**2.4. Optimization of Conditions for CIP Determination.** *2.4.1. Effect of the Incubation pH on the CIP Detection Performance.* For CIP sensing, the MIP/rGO/GCE electrode should rebind with CIP before the CIP determination via the DPV technique. In this study, the CIP solution was prepared by diluting a stock solution of CIP in 0.05 mol L$^{-1}$ phosphate buffer solution (PBS) at pH values ranging from 6.0 to 8.0, creating 1.0 × 10$^{-9}$ mol L$^{-1}$ of CIP. The electrode was further used in the electrochemical cell and operated in the DPV mode to obtain a responding current. Results were reported in the form of current variation ($\Delta I$), in which $\Delta I$ was defined as $I_0 - I_c$, a subtraction of baseline current ($I_0$) and corresponding current ($I_c$) (Figure S2a). The $\Delta I$ increased as the pH increased from 5.0 to 8.0 and was unaffected within a narrow pH range (6.5−7.0). Notably, although MIP/rGO/GCE was introduced into the incubation medium at different pH values, it was operated in a DPV mode in the medium of pH 6.5.[43−45]

*2.4.2. Incubation Time.* The effects of CIP incubation time on the response of the sensor were investigated by introducing MIP/rGO/GCE to 1.0 × 10$^{-9}$ mol L$^{-1}$ CIP solution at pH 6.5. The time was varied in the range of 1−20 min. As the time increased from 1 to 3, 5, and 7 min, the current variation ($\Delta I = I_0 - I_c$) increased from 37.65 to 49.46, 76.54, and 109.74 $\mu$A, respectively (Figure S2b). The $\Delta I$ plateaued as the rebinding time lasted longer than 8.0 min. The $\Delta I$ values were 110.37, 121.37, 116.18, 120.17, and 119.64, corresponding to the rebinding time of 10, 13, 15, 18, and 20 min, respectively. The
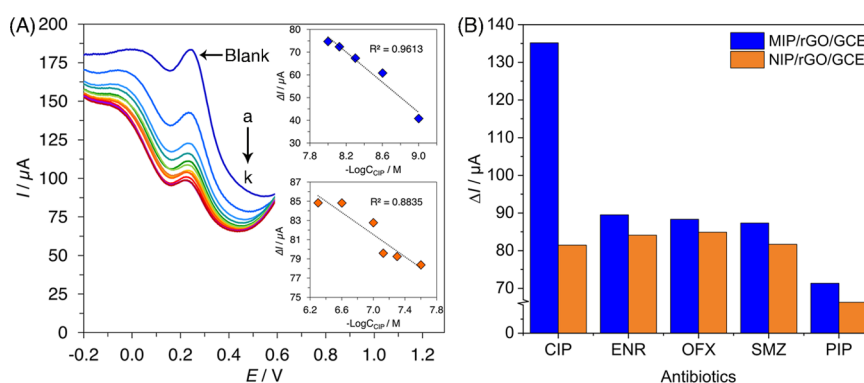
**Figure 6.** Performance of MIP/rGO/GCE sensor: (A) DPV of different CIP concentrations. Inset: plot of $\Delta I$ vs (a–k) logarithmic of $1.0 \times 10^{-9}$ to $5.0 \times 10^{-7}$ mol L$^{-1}$ CIP ($\Delta I$ = difference in peak current in absence and presence of the CIP) and (B) sensor selectivity upon introduction to $1.0 \times 10^{-6}$ mol L$^{-1}$ of CIP, ENR, OFX, SMZ, and PIP in PBS at pH 6.5.

**Table 1. Comparison of the MIP Analytical Techniques for the Detection of CIP**

| electrode | detection method | linear range ($\mu$mol L$^{-1}$) | LOD ($\mu$mol L$^{-1}$) | sensitivity ($\mu$A $\mu$mol$^{-1}$ L) | references |
|---|---|---|---|---|---|
| MIP microcantilever | dynamic | 1.5–150.9 | 0.8 | 2.6 Hz pg$^{-1}$ | 47 |
| Ch-AuMIP/GCE | DPV | 1–100 | 0.21 | $-47.6 \times 10^6$ | 48 |
| MIPs@SiO$_2$–FITC | fluorescent | 0.004–0.25 | 0.004 | | 49 |
| MMWCNTs@MIP/CPE | DPV | 0.005–0.85 | 0.0017 | 22.766 | 50 |
| MIP/PGE | SWV | 0.001–1000 | 0.000076 | $100 \times 10^6$ | 51 |
| MIP/rGO/GCE | DPV | 0.001–0.5 | 0.00005 | $5.78 \times 10^6$ | this study |

results state that adsorption sites on the MIP reach equilibrium at the CIP concentration of $1.0 \times 10^{-9}$ mol L$^{-1}$ after the incubation time of 7.0 min. An optimal incubation time of 7.0 min was used for this study.

## 2.5. Electrochemical Characteristics of MIP/rGO/GCE.

The redox characteristics of the MIP/rGO/GCE sensor were analyzed using CV analysis. The CV curves were acquired in a $[\text{Fe}(\text{CN})_6]^{3-/4-}$ mediator at scan rates ranging from 10 to 150 mV s$^{-1}$ (Figure 5A). Anodic and cathodic ($I_{pc}$) currents were monitored from the peaks of a CV curve and reported corresponding to the scan rate ($\nu^{1/2}$) (Figure 5B). The CV curves of the peak currents of the reduction and oxidation of $[\text{Fe}(\text{CN})_6]^{3-/4-}$ were plotted against the square roots of the scan rates ($I_{pa}$ vs $\nu^{1/2}$ and $I_{pc}$ vs $\nu^{1/2}$). The anodic and cathodic currents increased linearly with an increase in the scan rate. The correlations were: $I_{pa}$ ($\mu$A) = 3.19 $\nu^{1/2}$ + 11.48 ($R^2$ = 0.9900) and $I_{pc}$ ($\mu$A) = $-4.04$ $\nu^{1/2}$ $- 14.65$ ($R^2$ = 0.9814). The distinctive peaks of $I_{pa}$ and $I_{pc}$ indicated favorable electron transfer between MIP/rGO/GCE and $[\text{Fe}(\text{CN})_6]^{3-/4-}$ redox species. The characteristic of the MIP/rGO/GCE resembles that of a diffusion-controlled electrochemical reaction model, in which the sensing signal is directly proportional to the diffusion rate of the target analyte.

## 2.6. Analytical Performances toward CIP Detection.

The MIP/rGO/GCE sensor was operated in the DPV mode and introduced to CIP at different concentrations. The normalized peak current decreased as the CIP concentration increased (Figure 6A). The relation between the normalized current ($\Delta I$) and CIP concentration was linear over two dynamic ranges of the MIP/rGO/GCE sensor. The first range was at $1.0 \times 10^{-9}$ to $1.0 \times 10^{-8}$ mol L$^{-1}$ with a regression equation of $\Delta I$ ($\mu$A) = 33.27 log$C_{CIP}$ (M) + 342.86 with an $R^2$ of 0.9613. The second range was at $2.5 \times 10^{-8}$ to $5.0 \times 10^{-7}$ mol L$^{-1}$ with a regression equation of $\Delta I$ ($\mu$A) = 5.78 log$C_{CIP}$ (M) + 121.96 and a correlation coefficient ($R^2$) of 0.8835. An LOD was determined within a linear correlation range,

following the equation LOD = 3.3 SD/S, where SD is the standard deviation of the intercept and S is the slope of the calibration curve.[46] The sensitivity of 5.78 $\mu$A mol$^{-1}$ L ($n$ = 5) was obtained from the calibration plot of $\Delta I$ and log$C_{CIP}$. The LOD was $5.28 \times 10^{-11}$ mol L$^{-1}$, indicating that the sensor can detect the CIP of $5.28 \times 10^{-11}$ mol L$^{-1}$ with 95% confidence.

We compared our results with other MIP reports as summarized in Table 1 and other electrochemical methods in Table S1. Okan et al. developed MIP nanoparticles to modify a micromechanical cantilever sensor for CIP detection. The MIP microcantilever provided a sensitivity of 2.6 Hz pg$^{-1}$ with a LOD of 0.8 $\mu$mol L$^{-1}$ in the linear range of 1.5–150.9 $\mu$mol L$^{-1}$.[47] Surya et al. reported uses of chitosan-gold nanoparticle/MIP (Ch-AuMIP) to modify GCE for CIP detection. In the DPV mode, the sensor exhibited a LOD of 0.21 $\mu$mol L$^{-1}$ and sensitivity of $-47.6 \times 10^6$ $\mu$A $\mu$mol$^{-1}$ L within 1 to 100 $\mu$mol L$^{-1}$ of the linear response range.[48] Wu et al. synthesized MIP on fluorescein isothiocyanate-modified silica (MIPs@SiO$_2$-FITC). The detection was operated via the fluorescence techniques to obtain the LOD of 0.004 $\mu$mol L$^{-1}$ and a linear range of 0.004–0.25 $\mu$mol L$^{-1}$.[49] Bagheri et al. combined iron nanoparticles and MWCNT with MIP to synthesize magnetic MWCNT. The MWCNT–MIP composite was coated on the GCE. The electrode exhibited a LOD of 0.0017 $\mu$mol L$^{-1}$, a sensitivity of 22.766 $\mu$A $\mu$mol$^{-1}$ L, and a linear range of 0.005–0.85 $\mu$mol L$^{-1}$.[50] Yan et al. modified pencil graphite electrodes (PGE) with pyrrole and $o$-PDA MIP. In a square wave voltammetry (SWV) mode, the MIP/PGE provided a LOD of 0.000076 $\mu$mol L$^{-1}$ and a sensitivity of $100 \times 10^6$ $\mu$A $\mu$mol$^{-1}$ L in the linear range of 0.001–1000 $\mu$mol L$^{-1}$.[51] In this work, we synthesized the copolymer film of PANI and poly($o$-PDA) MIP on rGO/GCE using the electropolymerization process. The electrode was operated in the DPV mode, yielding a LOD of 0.00005 $\mu$mol L$^{-1}$, a sensitivity of $5.78 \times 10^6$ $\mu$A $\mu$mol$^{-1}$ L, and a linear range of 0.001–0.5 $\mu$mol L$^{-1}$.

**2.7. Reproducibility and Repeatability.** Five different MIP/rGO/GCE sensors ($n = 5$) were prepared independently under identical conditions and tested for the net current responses to $1.0 \times 10^{-9}$ mol L$^{-1}$ CIP. The responses were collected and compared to determine the reproducibility of sensor fabrication. The responses from the five sensors showed a relative standard deviation (RSD) of 4.9%, indicating good reproducibility of the fabrication process. The repeatability of the sensor was determined by averaging sensing responses five times from the same sensor to the same concentration of CIP ($1.0 \times 10^{-9}$ mol L$^{-1}$) (Figure S3). The sensor revealed an RSD of 0.5%, indicating good repeatability in accurate readouts without pretreatment.

**2.8. Selectivity of MIP/rGO/GCE.** The selectivity of the MIP/rGO/GCE sensor was examined by comparing the DPV response ($\Delta I$) to CIP in the presence of other interferences. The selected interferences in aquatic environments include antibiotic pollutants, such as ENR, OFX, SMZ, and PIP. The MIP/rGO/GCE sensors were fabricated and exposed to ENR, OFX, SMZ, and PIP at the same concentration of $1.0 \times 10^{-6}$ mol L$^{-1}$. Figure 6B displays the current intensity responses corresponding to CIP, ENR, OFX, SMZ, and PIP, in which the sensing response values to CIP are 1.5, 1.5, 1.6, and 1.9 times higher than those of ENR, OFX, SMZ, and PIP, respectively. The NIP-rGO/GCE sensor was tested as a control, revealing no sensing selectivity for the CIP compared to ENR, OFX, SMZ, and PIP. The imprinting factor ($\alpha$) and selectivity factor ($\beta$) were computed using eqs 2 and 3:

$$\alpha = \frac{\Delta I \ (\text{MIP})}{\Delta I \ (\text{NIP})} \tag{2}$$

$$\beta = \frac{\alpha_{\text{CIP}}}{\alpha_{\text{interferent}}} \tag{3}$$

Both factors provide information regarding the sensitivity of the sensor toward a target analyte as calculated in Table S2. The $\alpha$ suggests the superiority of MIP over NIP, whereas the $\beta$ focuses on the relative sensitivity of the target analyte over other interferences. The $\alpha$ for CIP, ENR, OFX, SMZ, and PIP are 1.7, 1.1, 1.0, 1.1, and 1.1, respectively. The $\alpha_{\text{CIP}}$ is significantly greater than the other antibiotics, indicating a high MIP/rGO/GCE sensitivity toward the target analyte (CIP). The $\beta$ for CIP, ENR, OFX, SMZ, and PIP are 1.0, 1.6, 1.6, 1.6, and 1.4, indicating that the sensor is more sensitive to CIP than other interference.

**2.9. Determination of CIP in Actual Water Samples.** The MIP/rGO/GCE sensor was designed to function as a real-time sensor for CIP detection. We investigated the performance of the sensor against tap and pond water samples. The diluted water solution (actual water: PBS; 1:5; v:v) was transferred to the electrochemical cell and spiked with different concentrations of CIP. Recovery tests were performed using DPV to determine CIP concentrations in water. The CIP concentration data from the sensor were compared with the actual concentrations in the water sample (Table S3). The precision of the sensor was determined using recovery (%), which is defined as the obtained data divided by the actual CIP concentration and multiplied by 100 (Table S3). For tap water, the recovery (%) of 84.2, 87.8, 87.1, and 87.8 corresponded to the CIP spike of 2.5, 5.0, 7.5, and 10.0 mol L$^{-1}$. The RSD remained less than 5% for all the data. For the pond water, the recovery (%) of 124.8, 123.4, 122.1, and 118.4 corresponded to the CIP spike of 2.5, 5.0, 7.5, and 10.0 mol L$^{-1}$. The RSD

was slightly higher than that of the tap water measurements and lower than 7.5% for all the data. Notably, the sensing data exhibited ~15% reduction for tap water and ~20% increment for pond water. This result requires further tests and analyses for water compositions and thus is part of our future experiments.

## 3. CONCLUSIONS

The MIP/rGO/GCE-based electrochemical sensor was synthesized by electropolymerization in the presence of a CIP molecular template. The copolymer film of PANI−o-PDA functions as the MIP with recognition sites for the CIP. Subsequently, an MIP/rGO composite was fabricated to promote carrier mobility. The sensor was operated in the DPV mode and exhibited high sensitivity and selectivity for CIP with good reproducibility and repeatability. Furthermore, key factors for the synthesis of MIP and CIP measurements were studied. The MIP/rGO/GCE sensor exhibited a high recovery rate, indicating a substantial potential to be used in realistic environments. Our future studies will focus on analyzing components in water samples, including surface water, groundwater, and tap water.

## 4. EXPERIMENTAL SECTION

**4.1. Chemicals and Reagents.** Graphite flakes (10 mesh, 99.9%) were purchased from Alfa Aesar (Tewksbury, USA). Sulfuric acid (H$_2$SO$_4$, analytical grade, 98%) was purchased from RCI Labscan Ltd. (Rongmuang, Thailand). Potassium permanganate (KMnO$_4$, 99.0%) and L-ascorbic acid (C$_6$H$_8$O$_6$, 99.0%) were purchased from Ajax Finechem Pty Ltd. (Seven Hills, Australia). Sodium nitrate (NaNO$_3$, Fluka Chemika, 99%), hydrogen peroxide (H$_2$O$_2$, Mercks, 30%), CIP (HPLC grade), ENR (HPLC grade), OFX (HPLC grade), SMZ (HPLC grade), and PIP (HPLC grade) were purchased from Sigma-Aldrich (St. Louis, USA) and used as received. Aniline (ANI, ACS reagent), o-PDA (HPLC grade), potassium ferricyanide (K$_3$Fe(CN)$_6$, ACS reagent), potassium ferrocyanide (K$_4$Fe(CN)$_6$·3H$_2$O, ACS reagent), potassium chloride (KCl, ReagentPlus), and N,N-DMF (C$_3$H$_7$NO, anhydrous) were obtained from Sigma-Aldrich (St. Louis, USA). Hydrochloric acid (HCl, ACS reagent, 37.0%), sodium hydroxide (NaOH, ACS reagent), and ethyl alcohol (C$_2$H$_5$OH, ACS reagent) were purchased from Merck (Darmstadt, Germany). The PBS (0.05 mol L$^{-1}$) was prepared by mixing solutions of potassium dihydrogen phosphate (KH$_2$PO$_4$, reagent grade) and dipotassium hydrogen phosphate (K$_2$HPO$_4$, reagent grade), which were purchased from Merck (Darmstadt, Germany). A stock solution of 0.1 mol L$^{-1}$ CIP was prepared by dissolving CIP in a 0.1 N HCl solution. All the aqueous solutions were prepared using UPW (Millipore water, USA, 18.2 MΩ cm$^{-1}$).

**4.2. Synthesis of Reduced Graphene Oxide.** rGO was supplied by the Nanocomposite Engineering (NanoCEN) Laboratory, Department of Chemical Engineering, Mahidol University. GO powder was synthesized following the chemical exfoliation method presented in a previous study.[37] Briefly, we mixed 2.0 g of graphite flakes with 1.0 g of NaNO$_3$ in 50 mL of H$_2$SO$_4$. The mixture was stirred in an ice bath at 0 °C for 2 h while 7.3 g of KMnO$_4$ was added. The mixture was transferred from the bath and stirred at 30 °C for 2.5 h. The viscous mixture was mixed with 55.0 mL of DI water and 7.0 mL of H$_2$O$_2$ to terminate the oxidation reaction. The mixture was

filtered using a vacuum filtration apparatus to obtain a brownish GO slurry. The GO was rinsed sequentially with 3% (v/v) HCl and DI water until the pH 7 supernatant was achieved. GO powder was dried in a vacuum oven at 60 °C for 24 h. For a synthesis of rGO, GO suspension (1.0 mg mL$^{-1}$) was prepared in an aqueous solution of 10 mg mL$^{-1}$ $C_6H_8O_6$. The mixture was stirred for 24 h to reduce GO to rGO. The rGO powder was obtained using a vacuum filtration apparatus, rinsed with DI water, and dried at 100 °C for 24 h. The powder was kept in a desiccator for future use.

**4.3. Preparation of the rGO/GCE.** The GCE (3 mm diameter carbon disk) was sequentially polished with 0.3, 0.1, and 0.05 $\mu$m alumina powder on polishing pads (CH Instruments, Inc.). It was rinsed with 1:1 HNO$_3$/H$_2$O (v/v), ethyl alcohol, and UPW, dried under a nitrogen stream, and heated to 60 °C for 10 min. The rGO suspension was prepared by suspending rGO (1.0 mg mL$^{-1}$) in UPW with assistance from ultrasonication. The rGO suspension of 5.0 $\mu$L was dropped on the GCE and further dried in an oven (Memmert, Schwabach, Germany) at 60 °C to create a uniform rGO film (1.42 $\mu$g mm$^{-2}$).

**4.4. Fabrication of MIP/GCE and NIP/GCE.** The rGO/GCE was employed in an electrochemical cell as a WE along with a counter electrode (CE, CHI115, CH Instruments Inc., Austin, USA) and reference electrode (RE, CHI111, CH Instruments Inc., USA). For the electropolymerization of MIP, the electrolyte was 1.0 × 10$^{-3}$ mol L$^{-1}$ ANI, 1.0 × 10$^{-3}$ mol L$^{-1}$ o-PDA, and 5.0 × 10$^{-3}$ mol L$^{-1}$ CIP as a template in a background medium of HCl solution (pH 3). The electropolymerization was performed in a cyclic voltammogram. A potential window of 0.0 to 0.7 V was applied to WE at 80 mV s$^{-1}$ scan rate for 15 cycles (Figure S4a). The MIP-modified electrode was eluted by immersion in 1.0 mol L$^{-1}$ HCl for 3 min, creating imprinted cavities on the MIP. MIP/rGO/GCE was thoroughly rinsed with UPW and stored in a desiccator for future use. In addition, NIP/rGO/GCE was fabricated following a similar procedure with no CIP during the electropolymerization. The CV curve obtained from the electropolymerization is illustrated in Figure S4b.

**4.5. Material Characterizations.** The physical, chemical, and crystallographic properties were analyzed using FE-SEM (JSM 7610F Plus, JEOL Ltd., Tokyo, Japan) equipped with an energy-dispersive X-ray spectrometer, FT-IR (Nicolet iS50 spectrometer, Thermo Fisher Scientific, Madison, USA), Raman spectroscopy (Jobin Yvon XploRA Plus, HORIBA, Kyoto, Japan), and XRD (D2 PHASER, Bruker, Bremen, Germany). For FE-SEM analysis, CIP, rGO, pre-elution MIP/rGO, and post-elution MIP/rGO were deposited in powder form on an adhesive carbon tape. The samples were dried in a vacuum oven sputter-coated with Pt (JEC-3000FC, JEOL, Tokyo, Japan) at 20 mA for 25 s for better visualization. CIP was sprinkled onto the grid and sputter-coated with Pt film. FE-SEM images were acquired using a 5.0 keV electron beam. FT-IR spectra were achieved over 4000−400 cm$^{-1}$ wavelength range, 4 cm$^{-1}$ resolution, and 64 scanning cycles per spectrum using the KBr-disc technique. The solid powder was diluted in KBr diluent and pressed using a Perkin Elmer hydraulic device at an applied pressure of five tons. Raman spectra were created in the 200−2000 cm$^{-1}$ range using Raman lasers of 532 nM at 0.70 mW and 785 nm at 7.18 mW. For XRD analysis, the spectra were recorded from a 5−90° (2$\theta$) window with a Cu-K$\alpha$ X-ray radiation source.

**4.6. Electrochemical Procedures.** The electrochemical studies were performed on a PalmSens4 Potentiostat/Galvanostat electrochemical system (PalmSens BV, Utrecht, The Netherlands) using a PSTrace 5.9 electrochemistry software PC interface. The sensitive element on the GCE was used as the WE, consisting of silver/silver chloride (Ag/AgCl) RE and platinum (Pt) wire CE. For the CV analysis, the sensor was scanned within a potential window of −0.2 to 0.6 V at a scan rate of 50 mV s$^{-1}$. An aqueous solution of 5.0 × 10$^{-3}$ mol L$^{-1}$ [Fe(CN)$_6$]$^{3-/4-}$ (1:1) and 0.1 mol L$^{-1}$ KCl was used as a medium. For the DPV experiment, the WE was applied with a step potential ($E_{step}$) of 5.0 mV, pulse potential ($E_{pulse}$) of 60.0 mV, pulse time ($t_{pulse}$) of 0.02 s, and at a scan rate of 50 mV s$^{-1}$. High-purity nitrogen gas was used for degassing the electrolyte medium for 10 min before the experiments. For the statistical analysis, we used regression analysis to determine key parameters for the sensor at the 95% confidence level. Precision of electrochemical analysis was quantified where $n$ = 5. The error bars of the results represent the SD of the mean by measurement.

**4.7. Preparation of Actual Water Samples.** Samples from the tap and pond water (13.796512N, 100.326857E) were collected during the summer time (April 8, 2022, 9:00 a.m.) at Mahidol University, Salaya campus, Thailand. The values of temperature (26.0 and 28.7 °C), pH (7.19 ± 0.17 and 8.11 ± 0.06), conductivity (0.28 and 0.88 mS cm$^{-1}$), salinity (0 and 0 g L$^{-1}$), and dissolved oxygen (2.0 and 0.5 mg L$^{-1}$) were averaged from three measurements for the tap and pond water, respectively. All samples were filtered with a glass fiber membrane (GF/B, 1.0 $\mu$m pore size, Whatman, U.K.) and diluted at a ratio of 1:5 in PBS (pH 6.5) to a total volume of 10.0 mL. CIP stock solutions were diluted to CIP-containing water samples with concentrations of 2.5, 5.0, 7.5, and 10.0 nM.

## ■ ASSOCIATED CONTENT

**ⓢ Supporting Information**

The Supporting Information is available free of charge at https://pubs.acs.org/doi/10.1021/acsomega.2c07095.

> It covers results from variation in synthesis parameter of the MIP/rGO/GCE; conditions for CIP sensing; CV from electropolymerization of MIP and NIP; comparison of the sensor with other electrochemical sensors; selectivity of the sensor; and signal recovery in actual water samples of the MIP/rGO/GCE sensor (PDF)

## ■ AUTHOR INFORMATION

**Corresponding Author**

**Suwanna Kitpati Boontanon** − *Graduate Program in Environmental and Water Resources Engineering, Department of Civil and Environmental Engineering, Faculty of Engineering, Mahidol University, Nakhon Pathom 73170, Thailand; Graduate School of Global Environmental Studies, Kyoto University, Kyoto 606-8501, Japan;* ⓞ orcid.org/0000-0003-2118-4577; Email: suwanna.boo@mahidol.ac.th

**Authors**

**Jedsada Chuiprasert** − *Graduate Program in Environmental and Water Resources Engineering, Department of Civil and Environmental Engineering, Faculty of Engineering, Mahidol*

*University, Nakhon Pathom 73170, Thailand;* ● orcid.org/
0000-0003-4507-7127

**Sira Srinives** − *Nanocomposite Engineering Laboratory (NanoCEN), Department of Chemical Engineering, Faculty of Engineering, Mahidol University, Nakhon Pathom 73170, Thailand;* ● orcid.org/0000-0002-7890-1103

**Narin Boontanon** − *Faculty of Environment and Resource Studies, Mahidol University, Nakhon Pathom 73170, Thailand*

**Chongrak Polprasert** − *Department of Civil Engineering, Faculty of Engineering, Thammasat University, Pathum Thani 12120, Thailand*

**Nudjarin Ramungul** − *National Metal and Materials Technology Center, National Science and Technology Development Agency, Pathum Thani 12120, Thailand*

**Napat Lertthanaphol** − *Nanocomposite Engineering Laboratory (NanoCEN), Department of Chemical Engineering, Faculty of Engineering, Mahidol University, Nakhon Pathom 73170, Thailand*

**Apisit Karawek** − *Nanocomposite Engineering Laboratory (NanoCEN), Department of Chemical Engineering, Faculty of Engineering, Mahidol University, Nakhon Pathom 73170, Thailand*

Complete contact information is available at:
https://pubs.acs.org/10.1021/acsomega.2c07095

## Author Contributions

J.C.: conceptualization, data curation, formal analysis, visualization, methodology, and writing—original draft and editing; S.S.: supervision, methodology, resources, investigation, and writing—review and editing; N.B.: methodology and supervision; C.P.: conceptualization and supervision; N.R.: funding acquisition and project administration; N.L.: resources; A.K.: formal analysis; and S.K.B.: supervision, formal analysis, funding acquisition, validation, and writing—review and editing.

## Notes

The authors declare no competing financial interest.

## ■ ABBREVIATIONS

ABR, antibiotic resistance; ANI, aniline; CE, counter electrode; CIP, ciprofloxacin; CV, cyclic voltammetry; DMF, dimethylformamide; DPV, differential pulse voltammetry; ENR, enrofloxacin; FQ, fluoroquinolone; FT-IR, Fourier transform infrared; GCE, glassy carbon electrode; HPLC, high-performance liquid chromatography; LOD, limit of detection; MIP, molecularly imprinted polymer; NIP, nonmolecular imprinted polymer; OFX, ofloxacin; o-PDA, o-phenylenediamine; PANI, polyaniline; PBS, phosphate buffer solution; PGE, pencil graphite electrode; PIP, piperacillin sodium salt; RE, reference electrode; rGO, reduced graphene oxide; RSD, relative standard deviation; SD, standard deviation; SMZ, sulfamethoxazole; SWV, square wave voltammetry; UPW, ultrapure water; WE, working electrode

## ■ REFERENCES

(1) Zhang, X.; Lin, B.; Li, X.; Wang, X.; Huang, K.; Chen, Z. MOF-derived magnetically recoverable Z-scheme $ZnFe_2O_4/Fe_2O_3$ perforated nanotube for efficient photocatalytic ciprofloxacin removal. *Chem. Eng. J.* 2022, 430, No. 132728.

(2) Yang, Y.-Y.; Zhao, J.-L.; Liu, Y.-S.; Liu, W.-R.; Zhang, Q.-Q.; Yao, L.; Hu, L.-X.; Zhang, J.-N.; Jiang, Y.-X.; Ying, G.-G. Pharmaceuticals and personal care products (PPCPs) and artificial sweeteners (ASs) in surface and ground waters and their application as indication of wastewater contamination. *Sci. Total Environ.* 2018, 616−617, 816−823.

(3) Carneiro, R. B.; Pozzi, E.; Corbi, J. J.; Zaiat, M. Ecotoxicity and antimicrobial inhibition assessment of effluent from an anaerobic bioreactor applied to the removal of sulfamethoxazole and ciprofloxacin antibiotics from domestic sewage. *Water, Air, Soil Pollut.* 2021, 232, 1−13.

(4) Sinthuchai, D.; Boontanon, S. K.; Boontanon, N.; Polprasert, C. Evaluation of removal efficiency of human antibiotics in wastewater treatment plants in Bangkok, Thailand. *Water Sci. Technol.* 2016, 73, 182−191.

(5) Sun, Y.; Dramou, P.; Song, Z.; Zheng, L.; Zhang, X.; Ni, X.; He, H. Lanthanide metal doped organic gel as ratiometric fluorescence probe for selective monitoring of ciprofloxacin. *Microchem. J.* 2022, 179, No. 107476.

(6) Bosma, R.; Devasagayam, J.; Singh, A.; Collier, C. M. Microchip capillary electrophoresis dairy device using fluorescence spectroscopy for detection of ciprofloxacin in milk samples. *Sci. Rep.* 2020, 10, 13548.

(7) Shevchenko, K. G.; Garkushina, I. S.; Canfarotta, F.; Piletsky, S. A.; Barlev, N. A. Nano-molecularly imprinted polymers (nanoMIPs) as a novel approach to targeted drug delivery in nanomedicine. *RSC Adv.* 2022, 12, 3957−3968.

(8) Han, S.; Yao, A.; Ding, Y.; Leng, Q.; Teng, F.; Zhao, L.; Sun, R.; Bu, H. A dual-template imprinted polymer based on amino-functionalized zirconium-based metal−organic framework for delivery of doxorubicin and phycocyanin with synergistic anticancer effect. *Eur. Polym. J.* 2022, 170, No. 111161.

(9) Wang, G. N.; Yang, K.; Liu, H. Z.; Feng, M. X.; Wang, J. P. Molecularly imprinted polymer-based solid phase extraction combined high performance liquid chromatography for determination of fluoroquinolones in milk. *Anal. Methods* 2016, 8, 5511−5518.

(10) de Oliveira, H. L.; da Silva Anacleto, S.; da Silva, A. T. M.; Pereira, A. C.; de Souza Borges, W.; Figueiredo, E. C.; Borges, K. B. Molecularly imprinted pipette-tip solid phase extraction for selective determination of fluoroquinolones in human urine using HPLC-DAD. *J. Chromatogr., B* 2016, 1033−1034, 27−39.

(11) Li, X.; Chen, X.; Lv, Z.; Wang, B. Ultrahigh ciprofloxacin accumulation and visible-light photocatalytic degradation: Contribution of metal organic frameworks carrier in magnetic surface molecularly imprinted polymers. *J. Colloid Interface Sci.* 2022, 616, 872−885.

(12) Tang, M.; Wan, J.; Wang, Y.; Yan, Z.; Ma, Y.; Sun, J.; Ding, S. Developing a molecularly imprinted channels catalyst based on template effect for targeted removal of organic micropollutants from wastewaters. *Chem. Eng. J.* 2022, 445, No. 136755.

(13) Wang, Y.; Cheng, J.; Liu, X.; Ding, F.; Zou, P.; Wang, X.; Zhao, Q.; Rao, H. $C_3N_4$ Nanosheets/metal−organic framework wrapped with molecularly imprinted polymer sensor: fabrication, characterization, and electrochemical detection of furosemide. *ACS Sustainable Chem. Eng.* 2018, 6, 16847−16858.

(14) Sullivan, M. V.; Henderson, A.; Hand, R. A.; Turner, N. W. A molecularly imprinted polymer nanoparticle-based surface plasmon resonance sensor platform for antibiotic detection in river water and milk. *Anal. Bioanal. Chem.* **2022**, *414*, 3687−3696.

(15) Çorman, M. E.; Ozcelikay, G.; Cetinkaya, A.; Kaya, S. I.; Armutcu, C.; Özgür, E.; Uzun, L.; Ozkan, S. A. Metal-organic frameworks as an alternative smart sensing platform for designing molecularly imprinted electrochemical sensors. *TrAC, Trends Anal. Chem.* **2022**, *150*, No. 116573.

(16) Zhang, Z.; Huang, L.; Sheng, S.; Jiang, C.; Wang, Y. MIL-125 (Ti)-derived COOH functionalized $TiO_2$ grafted molecularly imprinted polymers for photoelectrochemical sensing of ofloxacin. *Sens. Actuators, B* **2021**, *343*, No. 130119.

(17) Singh, C.; Ali, M. A.; Reddy, V.; Singh, D.; Kim, C. G.; Sumana, G.; Malhotra, B. Biofunctionalized graphene oxide wrapped carbon nanotubes enabled microfluidic immunochip for bacterial cells detection. *Sens. Actuators, B* **2018**, *255*, 2495−2503.

(18) Xing, W.; Yan, Y.; Wang, C.; Gao, J.; Yu, C.; Yan, Y.; Li, C.; Ma, Z.; Wu, Y. MOFs self-assembled molecularly imprinted membranes with photoinduced regeneration ability for long-lasting selective separation. *Chem. Eng. J.* **2022**, *437*, No. 135128.

(19) Wang, Y.; Sun, X.; Cai, L.; Wang, H.; Zhang, B.; Fang, G.; Wang, S. A "signal on/off" biomimetic electrochemiluminescence sensor using titanium carbide nanodots as co-reaction accelerator for ultra-sensitive detection of ciprofloxacin. *Anal. Chim. Acta* **2022**, *1206*, No. 339690.

(20) Abo-Elmagd, I. F.; Mahmoud, A. M.; Al-Ghobashy, M. A.; Nebsen, M.; El Sayed, N. S.; Nofal, S.; Soror, S. H.; Todd, R.; Elgebaly, S. A. Impedimetric sensors for Cyclocreatine phosphate determination in plasma based on Electropolymerized poly (*o*-phenylenediamine) molecularly imprinted polymers. *ACS Omega* **2021**, *6*, 31282−31291.

(21) Yahyapour, M.; Ranjbar, M.; Mohadesi, A. Determination of ciprofloxacin drug with molecularly imprinted polymer/co-metal organic framework nanofiber on modified glassy carbon electrode (GCE). *J. Mater. Sci.: Mater. Electron.* **2021**, *32*, 3180−3190.

(22) Jiang, Z.; Li, G.; Zhang, M. A novel sensor based on bifunctional monomer molecularly imprinted film at graphene modified glassy carbon electrode for detecting traces of moxifloxacin. *RSC Adv.* **2016**, *6*, 32915−32921.

(23) El Azab, N. F.; Mahmoud, A. M.; Trabik, Y. A. Point-of-Care Diagnostics for Therapeutic Monitoring of Levofloxacin in Human Plasma Utilizing Electrochemical Sensor Mussel-Inspired Molecularly Imprinted Copolymer. *J. Electroanal. Chem.* **2022**, *918*, No. 116504.

(24) Marmisollé, W. A.; Azzaroni, O. Recent developments in the layer-by-layer assembly of polyaniline and carbon nanomaterials for energy storage and sensing applications. From synthetic aspects to structural and functional characterization. *Nanoscale* **2016**, *8*, 9890−9918.

(25) Fenoy, G. E.; Van der Schueren, B.; Scotto, J.; Boulmedais, F.; Ceolín, M. R.; Bégin-Colin, S.; Bégin, D.; Marmisollé, W. A.; Azzaroni, O. Layer-by-layer assembly of iron oxide-decorated few-layer graphene/PANI: PSS composite films for high performance supercapacitors operating in neutral aqueous electrolytes. *Electrochim. Acta* **2018**, *283*, 1178−1187.

(26) Mitra, R.; Saha, A. Engineering. Reduced graphene oxide based "turn-on" fluorescence sensor for highly reproducible and sensitive detection of small organic pollutants. *ACS Sustainable Chem. Eng.* **2017**, *5*, 604−615.

(27) Pham, T. S. H.; Mahon, P. J.; Lai, G.; Yu, A. Reduced graphene oxide nanocomposite modified electrodes for sensitive detection of ciprofloxacin. *Electroanalysis* **2018**, *30*, 2185−2194.

(28) Fu, L.; Mao, S.; Chen, F.; Zhao, S.; Su, W.; Lai, G.; Yu, A.; Lin, C.-T. Graphene-based electrochemical sensors for antibiotic detection in water, food and soil: a scientometric analysis in CiteSpace (2011−2021). *Chemosphere* **2022**, *297*, No. 134127.

(29) Goyal, A.; Sakata, T. Development of a Redox-Label-Doped Molecularly Imprinted Polymer on *β*-Cyclodextrin/Reduced Gra-

phene Oxide for Electrochemical Detection of a Stress Biomarker. *ACS Omega* **2022**, *7*, 33491−33499.

(30) Pienutsa, N.; Yannawibut, K.; Phattharaphongmanee, J.; Thonganantakul, O.; Srinives, S. Titanium dioxide-graphene composite electrochemical sensor for detection of hexavalent chromium. *Int. J. Miner., Metall. Mater.* **2022**, *29*, 529−535.

(31) Reddy, Y. V. M.; Shin, J. H.; Palakollu, V. N.; Sravani, B.; Choi, C.-H.; Park, K.; Kim, S.-K.; Madhavi, G.; Park, J. P.; Shetti, N. P. Strategies, advances, and challenges associated with the use of graphene-based nanocomposites for electrochemical biosensors. *Adv. Colloid Interface Sci.* **2022**, *304*, No. 102664.

(32) Bard, A. J.; Faulkner, L. R.; White, H. S. *Electrochemical methods: fundamentals and applications*; John Wiley & Sons, 2022.

(33) Liu, H.; Xie, M.; Pan, B.; Li, N.; Zhang, J.; Lu, M.; Luo, J.; Wang, H. In-situ intercalated pyrolytic graphene/serpentine hybrid as an efficient lubricant additive in paraffin oil. *Colloids Surf., A* **2022**, *652*, No. 129929.

(34) Gicevicius, M.; Kucinski, J.; Ramanaviciene, A.; Ramanavicius, A. Tuning the optical pH sensing properties of polyaniline-based layer by electrochemical copolymerization of aniline with o-phenylenediamine. *Dyes Pigm.* **2019**, *170*, 107457.

(35) Al-Hussaini, A. S.; Elias, A. M.; El-Ghaffar, A.; Mahmoud, A. New poly (aniline-co-*o*-phenylenediamine)/kaolinite microcomposites for water decontamination. *J. Polym. Environ.* **2017**, *25*, 35−45.

(36) Zhou, T.; Wu, S.; Cai, J.; Ruan, W. Rapid humidity sensors based on poly (o-phenylenediamine-co-aniline) spherical nanoparticles. *Polym. Bull.* **2020**, *77*, 1095−1105.

(37) Pienutsa, N.; Roongruangsree, P.; Seedokbuab, V.; Yannawibut, K.; Photoomvijitwong, C.; Srinives, S. $SnO_2$-graphene composite gas sensor for a room temperature detection of ethanol. *Nanotechnology* **2021**, *32*, 115502.

(38) Ye, F.; Zhao, B.; Ran, R.; Shao, Z. A polyaniline-coated mechanochemically synthesized tin oxide/graphene nanocomposite for high-power and high-energy lithium-ion batteries. *J. Power Sources* **2015**, *290*, 61−70.

(39) Mosali, V. S. S.; Bowmaker, G. A.; Gerard, M.; Kilmartin, P. A.; Travas-Sejdic, J.; Zujovic, Z. D. Self-assembled centimetre-sized rods obtained in the oxidation of *o*-phenylenediamine and aniline. *Polym. Int.* **2015**, *64*, 1135−1141.

(40) Lan, H.; Muslim, A.; Hojiahmat, M.; Wang, L.; Meng, Y.; Zhong, Q. Morphology formation mechanism and electrochemical performance of poly (*o*-phenylenediamine) based electrode materials. *Synth. Met.* **2021**, *273*, No. 116688.

(41) Nugrahani, I.; Tjengal, B.; Gusdinar, T.; Horikawa, A.; Uekusa, H. A comprehensive study of a new 1.75 hydrate of ciprofloxacin salicylate: SCXRD structure determination, solid characterization, water stability, solubility, and dissolution study. *Crystals* **2020**, *10*, 349.

(42) Antilén, M.; Valencia, C.; Peralta, E.; Canales, C.; Espinosa-Bustos, C.; Escudey, M. Enrofloxacin behavior in presence of soil extracted organic matter: an electrochemical approach. *Electrochim. Acta* **2017**, *244*, 104−111.

(43) Yuphintharakun, N.; Nurerk, P.; Chullasat, K.; Kanatharana, P.; Davis, F.; Sooksawat, D.; Bunkoed, O. A nanocomposite optosensor containing carboxylic functionalized multiwall carbon nanotubes and quantum dots incorporated into a molecularly imprinted polymer for highly selective and sensitive detection of ciprofloxacin. *Spectrochim. Acta, Part A* **2018**, *201*, 382−391.

(44) Feng, X.; Cheng, H.; Pan, Y.; Zheng, H. Development of glucose biosensors based on nanostructured graphene-conducting polyaniline composite. *Biosens. Bioelectron.* **2015**, *70*, 411−417.

(45) Jalal, N. R.; Madrakian, T.; Afkhami, A.; Ghamsari, M. Polyethylenimine@ $Fe_3O_4$@ carbon nanotubes nanocomposite as a modifier in glassy carbon electrode for sensitive determination of ciprofloxacin in biological samples. *J. Electroanal. Chem.* **2019**, *833*, 281−289.

(46) Beluomini, M. A.; da Silva, J. L.; Sedenho, G. C.; Stradiotto, N. R. D-mannitol sensor based on molecularly imprinted polymer on

electrode modified with reduced graphene oxide decorated with gold nanoparticles. *Talanta* **2017**, *165*, 231−239.

(47) Okan, M.; Sari, E.; Duman, M. Molecularly imprinted polymer based micromechanical cantilever sensor system for the selective determination of ciprofloxacin. *Biosens. Bioelectron.* **2017**, *88*, 258−264.

(48) Surya, S. G.; Khatoon, S.; Lahcen, A. A.; Nguyen, A. T.; Dzantiev, B. B.; Tarannum, N.; Salama, K. N. A chitosan gold nanoparticles molecularly imprinted polymer based ciprofloxacin sensor. *RSC Adv.* **2020**, *10*, 12823−12832.

(49) Wu, C.; Cheng, R.; Wang, J.; Wang, Y.; Jing, X.; Chen, R.; Sun, L.; Yan, Y. Fluorescent molecularly imprinted nanoparticles for selective and rapid detection of ciprofloxacin in aquaculture water. *J. Sep. Sci.* **2018**, *41*, 3782−3790.

(50) Bagheri, H.; Khoshsafar, H.; Amidi, S.; Ardakani, Y. H. Fabrication of an electrochemical sensor based on magnetic multi-walled carbon nanotubes for the determination of ciprofloxacin. *Anal. Methods* **2016**, *8*, 3383−3390.

(51) Yan, C.; Li, J.; Meng, T.; Liu, X.; Zhang, R.; Chen, Y.; Wang, G. Selective recognition of ciprofloxacin hydrochloride based on molecular imprinted sensor via electrochemical copolymerization of pyrrole and o-phenylenediamine. *Int. J. Electrochem. Sci.* **2016**, *11*, 6466−6476.